Optical Engineering

OpticalEngineering.SPIEDigitalLibrary.org

Lensless fiber-deployed low-coherence interferometer for *in-situ* measurements in nonideal environments

Tom Hovell
Ranveer S. Matharu
Jon Petzing
Laura Justham
Peter Kinnell

SPIE.

Tom Hovell, Ranveer S. Matharu, Jon Petzing, Laura Justham, Peter Kinnell, "Lensless fiber-deployed low-coherence interferometer for *in-situ* measurements in nonideal environments," *Opt. Eng.* **59**(1), 014113 (2020), doi: 10.1117/1.OE.59.1.014113

Lensless fiber-deployed low-coherence interferometer for *in-situ* measurements in nonideal environments

Tom Hovell,* **Ranveer S. Matharu, Jon Petzing, Laura Justham, and Peter Kinnell**
Loughborough University, Wolfson School of Mechanical, Electrical and
Manufacturing Engineering, Loughborough, United Kingdom

Abstract. Low-coherence interferometry (LCI) is a well-established optical method used for obtaining geometric measurements, suited for operating in nonideal environments as shown through its use in biomedical science, where it is referred to as optical coherence tomography. However, work on characterizing these technologies' ability to work *in-situ* within the area of manufacturing is yet to be demonstrated. This research is motivated by the need to develop robust sensors capable of operating in the harsh environment of manufacturing processes in near real-time, providing on-demand process control for the next generation of precise, and highly adaptive schemes of production. The evaluation of a common-path, lensless, spectral-domain, LCI-based sensor for measurements of step heights in air and in the nonideal operating environment of water is demonstrated. Calibration experiments have explored linearity of measurements over a 1-mm investigated axial range with deviations of the order of ±50 nm in air and ±100 nm in water. Step heights of 8, 7, 6, and 5 μm were measured in air and also with the sample and sensing probe submerged in water. Step heights in both media closely align with calibrated specifications given by the manufacturer demonstrating submicrometer accuracy and a precision of ±56 nm in air and ±76 nm in water. [DOI: 10.1117/1.OE.59.1.014113]

Keywords: metrology; interferometry; fiber optics.

Paper 191477 received Oct. 23, 2019; accepted for publication Dec. 26, 2019; published online Jan. 28, 2020.

1 Introduction

Precise, accurate, and timely measurements of part dimensions are essential for controlling manufacturing processes and are critical for ensuring the desired quality of products is achieved and maintained. This is increasingly important to support the manufacture of high-value components with complex microscale geometric and surface texture requirements. To support the manufacture of such challenging products, measurement data have traditionally been collected using off-line postprocess verification steps, in which parts are taken to an inspection station or measurement lab for checking. Although limited, using this approach does allow for nonconforming parts to be identified and in some cases allows for rework to avoid scrapping parts. However, as processes are pushed to their limits and demands for accuracy and precision increase, there is a clear need to reduce the reliance on postprocess verification and instead make more use of *in-situ* measurements.

If measurement data are collected during a process with the part *in-situ*, then it is easier to provide feedback control for the process. The problem is that many high precision measurement technologies are not suitable for close *in-situ* integration with manufacturing processes. Process environments are often highly space constrained and are subject to conditions that are deemed nonideal for many traditional measurement instruments. For example, there is often liquid and or other contaminates present, thermal gradients, vibration, and electromagnetic interference. Current industrial measurement instruments have been designed for operation within an environmentally controlled metrology laboratory, and as such are not suited for direct application to

---

*Address all correspondence to Tom Hovell, E-mail: T.Hovell@lboro.ac.uk on-machine measurement during machining. Their large size, and inability to cope with vibration, thermal change, and contaminants encountered during manufacturing are significant barriers to close integration. Alternative approaches to measurement are, therefore, required that make use of sensor technology that is inherently more suitable for close integration within the process environment.

Low-coherence interferometry (LCI) is a useful noncontact optical technology capable of performing high precision absolute depth measurements in a wide range of challenging, space constrained environments, as shown through its use in the field of biomedical science where it is also known as optical coherence tomography[1] and is used to provide tomographic depth measurements of features on skin or within the human body. The use of LCI-based sensors in fields more related to manufacturing has also been presented in literature, for example, for analyzing pharmaceutical film coatings,[2] tracking thin-film growth,[3] and the inspection of surface topography.[4–10] LCI benefits from easy integration with fiber optics, allowing sensors to be located *in-situ* and at a distance from the readout sensor and electronics, meaning only the chemically inert, extremely compact, and robust optical fiber needs to be integrated within the manufacturing process environment. These characteristics make LCI particularly interesting for *in-situ* measurement where integration using other sensor technology is currently not possible. For example, in electrochemical jet machining (EJM), which is a novel process for creating multiscale (micrometer to millimeter) surface geometries and textures using a small electrode nozzle with an inner diameter of the order 150 to 1000 μm.[11] In EJM, a liquid electrolyte jet is used to form an electrochemical cell between the electrode nozzle and the workpiece. For effective *in-situ* measurements to support process control in EJM, a sensor must be positioned within the liquid jet; therefore, LCI using a lensless configuration is one of the few sensing elements capable of integration into the electrode nozzle.

Previous work has observed the use of lensless LCI for application to near-field biological measurements in nonideal operating conditions.[9,10] However, to allow for useful progression of lensless fiber-deployed LCI sensors to on-machine measurement, performance characterization in ideal and degradation of sensing abilities in nonideal modes is required. In addition, previous work observes near-field imaging; yet in the case of machining or manufacturing procedures, the ability to measure across an extended range of operation is required. Quantification of the sensor performance between ideal and nonideal operating domains to the authors knowledge has yet to be demonstrated.

LCI as a sensor technology has significant potential; however, limited work has evaluated its performance for high accuracy and precision measurements within a manufacturing context. In this work, an in-depth evaluation of the performance characteristics of a common-path, lensless, fully fiber-enclosed LCI sensor for geometric and depth measurements of metallic samples in air and submerged in water is presented. The results demonstrate the performance ability of the sensor operating in nonideal conditions over a 1-mm range. Step height measurements are completed in both media with the determination of operation linearity with accuracy and precision achievable.

2 Method

2.1 *Experimental Setup*

The optomechanical experimental setup is shown in Fig. 1, whereby a fully fiber-enclosed based implementation of an LCI with a common path is used for both the reference and sample signal leg, taking advantage of reduced sensitivity to vibrations, thermal fluctuations, and humidity, and removing the requirement for dispersion compensation between signals.[12] A spectral- or Fourier-domain approach is implemented due to advantages of high acquisition speed and sensitivity over time-domain methods as reported by Leitgeb et al.[13] The system was designed to be unlensed with the bare cleaved fiber having a numerical aperture of 0.13. This provides a micrometer-level footprint and form factor of the sensor, to explore whether reliable measurement across varying depth was still possible. The system in this configuration has a confocal parameter of 83.5 μm and a $1/e^2$ transverse resolution of 5 μm.

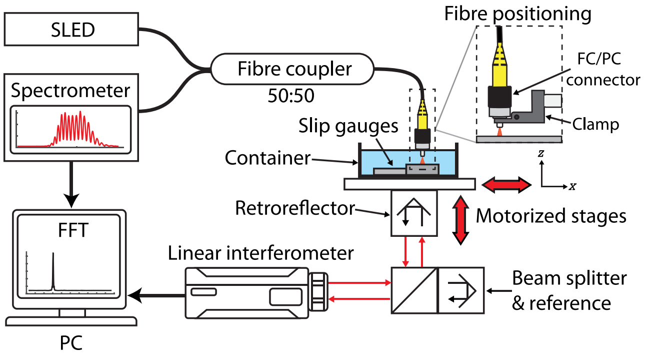

Fig. 1 Experimental setup of common-path LCI.

As shown in Fig. 1, the system consists of a broadband light source provided by a superluminescent diode (EXS210068-01, Beratron, 850 nm) with a 3-dB bandwidth of 58 nm and an emitting power of 5.14 mW at 160 mA. A single-mode fiber coupler with a splitting ratio of 50:50 for beam splitting and coupling was used, with only one branch of signal output being used as the common path for the signal and reference. A spectrometer (MayaPro2000, Ocean Optics) operating at 125 Hz with a 2048×64 pixel array, starting wavelength of 756 nm and spectral range of 174 nm with a resolution of 0.21 nm was used, giving a theoretical axial operating range of ∼2.15 mm before aliasing, as defined from Eq. (1).[14]

$$z_{\max} = \left(\frac{\lambda_0^2}{4}\right)\left(\frac{N_s}{\Delta\lambda}\right), \tag{1}$$

where N_s is the number of pixels for which the light source spectrum at full-width half-maximum $\Delta\lambda$ is sampled across. Here, λ_0 denotes the light source center frequency.

A fiber clamp was used to hold the end of the single-mode fiber (780HP with FC/PC connector) perpendicular to the object target (slip gauges), and stand-off distance was minimized to prevent signal decay with increased imaging depth due to the highly divergent nature of light exiting the fiber tip, as reported by Liu et al.[15]

To perform scanning measurements on samples, a set of three-axis stepper motor-driven translation stages (MFA-PPD, Newport) were used. The stages have a minimum incremental motion of 0.1 μm in each of the XYZ directions with typical accuracies in the range of ± 0.9 μm and were driven from a three-axis motion controller and driver (ESP 301, Newport) controlled by a custom-made LabVIEW program. The same LabVIEW program was used to simultaneously acquire spectra from the spectrometer and during calibration procedures positional data from a laser interferometer reference (XL-80, Renishaw) (Fig. 1).

To experimentally evaluate the performance of the system for in-process measurements, a series of step height measurements have been performed by traversing laterally across a pair of tungsten carbide slip gauges (OPUS, Cornwall, United Kingdom), as described in Fig. 1.

2.2 *Working Principles*

The theoretical principles of LCI have been detailed in literature for an object with N discrete back-scattering reflectors.[14,16] The signal obtained by the spectrometer is shown in Eq. (2) where the photocurrent is generated by a square-law detector expressed as a function of spatial frequency also known as wavenumber k. This represents a modulated signal term riding on top of the reference signal or "DC term" as it is often referred to as shown in Fig. 3(a).

$$I_D(k) = \frac{\rho}{4}S(k)\left[R_R + \sum_{n=1}^{N} R_{Sn}\right] + \frac{\rho}{2}\left[S(k)\sum_{n=1}^{N}\sqrt{R_R R_{Sn}}(\cos[2kn(z_R - z_{Sn})])\right] + \frac{\rho}{4}\left[S(k)\sum_{n\neq m=1}^{N}\sqrt{R_{Sn}R_{Sm}}(\cos[2kn(z_{Sn} - z_{Sm})])\right], \tag{2}$$

where I_D is the photocurrent generated by the spectrometer, ρ is the responsivity of the line scan camera, $S(k)$ is the spectral power density of the source as a function of wavenumber, R_R is the reflectance of the reference, R_S is the reflectance of the sample reflector, and $2(z_R - z_{Sn})$ is the round trip optical path difference (OPD) between the reference and n'th sample reflector located at a distance of z_{Sn}. Here, $2(z_{Sn} - z_{Sm})$ is the round trip OPD between the reference and n'th and m'th sample reflector.

In this work, measurement of metallic surfaces is completed, which provides a single sample reflector ($N = 1$), allowing for reduction of Eq. (2) to the form shown in Eq. (3). This removes the interference noise, which occurs between reflectors at different OPDs for $N > 1$.

$$I_D(k) = \frac{\rho}{4} S(k)[R_R + R_{S1}] + \frac{\rho}{2} S(k)\left[\sqrt{R_R R_{S1}}(\cos[2kn(z_R - z_{S1})])\right], \tag{3}$$

Depth information can be obtained by performing an inverse Fourier transform on Eq. (3) to form Eq. (4).

$$i_D(z) = \frac{\rho}{8}\gamma(z)[R_R + R_{S1}] + \frac{\rho}{4}\gamma(z) \otimes \left[\sqrt{R_R R_{S1}}(\delta[(z \pm 2n(z_R - z_{S1})])\right], \tag{4}$$

where $i_D(z)$ is the intensity recorded as a function of OPD, and $\gamma(z) = FT\{S(k)\}$ is the coherence function.

2.3 *Signal Processing*

In LCI, where spectra are captured by a CCD or CMOS array, the signal is approximately uniformly sampled by wavelength due to the diffractive nature of the spectrometer used. However, fast Fourier transform (FFT) algorithms are most efficient when the data points are evenly spaced within the frequency domain.[17] Due to the relationship between wavenumber and wavelength, (λ), ($k = 2\pi/\lambda$), the data will be nonuniformly spaced by wavenumber, requiring a resampling process before a conventional FFT can be effectively applied[18] as seen in Eqs. (3) and (4). If the dataset is left as linear in λ before the FFT is applied, then severe deterioration of axial resolution and signal-to-noise ratio (SNR) will be present in the signal, with an OPD-dependent broadening of the point spread function leading to a reduced operational limit due to signal fall-off,[18] this phenomena can be seen in Fig. 2.

It is possible to avoid this requirement for resampling of the data using a nonuniform direct Fourier transform (NuDFT) instead of an FFT algorithm. However, the NuDFT is more computationally intensive than other alternatives for resampling.[19] Since computational time is particularly important for high-speed imaging, the FFT is preferred. Resampling approaches can be categorized into two methods; (1) use of a special hardware configuration that samples the returned signal directly to be linear in k.[20,21] However, these methods also add additional cost, design complexity, and are not easily translated between systems. (2) Or use of a software–based method, acquiring the signal nonlinearly in k and resampling it during postprocessing through the use of a λ to k-mapping function.[15,22–29] However, literature shows that for software-based methods, the interpolation is not as good for reflectors close to the maximum achievable depth (Nyquist limit) due to high–frequency fringes in the interferogram that are poorly sampled.[30]

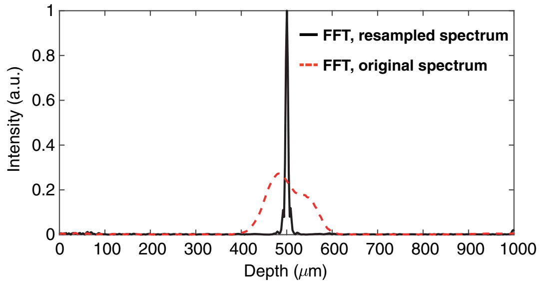

Fig. 2 Comparison between FFT of resampled spectrum and FFT of original spectrum.

Methods of circumventing remapping captured spectra through various computational techniques have also been investigated in literature.[31–33]

The approach taken in this work is similar to that presented for automatic calibration[15] and interferometric methods,[23–25] relying on the knowledge that for a singular reflector, and while operating in a common-path configuration negating the requirement for dispersion compensation, the interference fringes will be evenly spaced in k-space. By using zero-crossing detection, fringe spacing as a function of pixel number is obtained from which a mapping relationship between linear in λ and linear in k-space can be created, this allows interpolation of the data using a B-spline interpolation to create an evenly sampled dataset in k-space before performing an FFT. To relate the Fourier transformed signal to a spatial distance, a further calibration step was carried out as explained in Sec. 3.

To remove the DC term, it is a common practice to perform a high-pass filter on the captured spectra. This method removes the ability to analyze very small OPD's however, or leaves possible measurement ambiguity if not fully removed especially at higher OPD where the SNR of the system is comparatively small. In effect, the full removal of this term leads to a region of $\sim 32\ \mu\mathrm{m}$ that would be unresolvable in this setup though application of a high-pass cut-off filter. The method used to remove the DC-term from obtained signal in this work is outlined in Fig. 3. The DC-term was extracted from the raw signal shown in Fig. 3(a) by finding the mid-point between the upper and lower envelope of the spectrum using MATLAB's V2018 envelope function shown in Fig. 3(b), subtraction of this envelope mid-point from the original signal is then performed to get access to only the interference fringes as shown in Fig. 3(c).

To determine the interval of $k(\delta k)$ of the spectrometer for a CCD array of N pixels, the maximum measurable OPD before aliasing occurs due to the Nyquist criteria can be calculated from Eq. (1). From this, it can be seen that the z axis will go from $-\pi/2\delta k$ to $\pi/2\delta k$ in steps of $\pi/N\delta k = \pi/\Delta k$ such that a peak located at pixel N_i on the spectrometer reading will correspond to a depth shown in Eq. (5).

$$z_i = \left(\frac{\pi}{\delta k}\right)\left(\frac{N_i}{N}\right). \tag{5}$$

To calibrate the LCI system, sensor readings were obtained simultaneously with a reference measurement provided by a Renishaw XL-80 laser interferometer, as explained in Sec. 3, allowing accurate determination of δk and Δk.

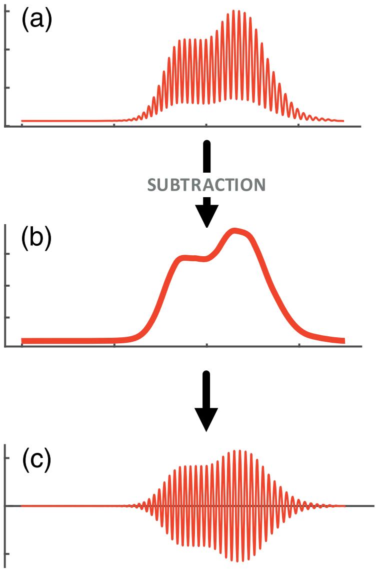

Fig. 3 Illustrative signal processing steps: (a) raw captured spectrum, (b) profile at the mid-point between upper and lower envelope, and (c) spectrum after removing the envelope profile—removes the DC term.

3 Sensor Calibration

To relate peak frequency obtained from a measured sample offset from the fiber tip to a spatial distance, a calibration procedure was performed. To calibrate the sensor, a flat mirrored sample surface was translated vertically using the z axis stepper motor-driven translation stage while simultaneously being measured by both the LCI system and the Renishaw XL-80 interferometer (accuracy assured to ± 0.5 μm per meter) to act as a traceable reference measurement. The sample was translated in steps of 10 μm for a total distance of 1000 μm with four repetitions of the experiment being completed in air and water with the data displayed showing the mean value of the results. By fitting a first-order polynomial to the LCI versus XL-80 dataset, an approximate linear relationship was observed. Upon closer inspection of the residual error from the fit (Fig. 4), it can be seen that a standard deviation of $\sim$50 nm is present in air and $\sim$100 nm in water over the measured offset rang. This relationship between LCI sensor measurement (FFT peak locations) and spatial depth supplied by the XL-80 allows for quantification of distance at any sample path length.

If higher order polynomial fits are applied to the LCI versus Renishaw dataset, then the residual error curve becomes increasingly flattened, improving the polynomial fit to the data over the measured range as shown in the box plot diagrams (Fig. 5 and Table 1). Here, the box plots demonstrate an approximately Gaussian distribution of residual error with the whiskers covering $\pm \sim 2.7\sigma$ of the dataset with outliers shown from the crosses.

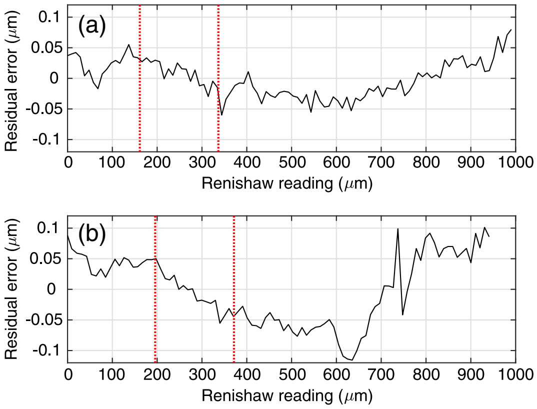

Fig. 4 Residual errors from first-order polynomial fit to LCI captured readings versus Renishaw XL-80 readings across measured offset range, in (a) air and (b) submerged sample/fiber tip in water, the dotted vertical lines show the operating range in which step height measurements were taken.

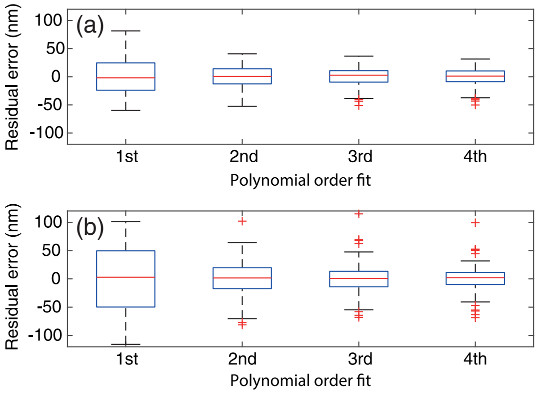

Fig. 5 Residual errors for first-, second-, third-, and fourth-order polynomial fits to LCI captured readings versus Renishaw XL-80 readings in (a) air and (b) submerged in water. The red "+" symbols indicate outlier values.

Table 1 Comparison of residual error from the best-fit line for first-, second-, third-, and fourth-order polynomial fits.

		Polynomial fit			
Environment		First	Second	Third	Fourth
Air (nm)	Max	82	53	51	50
	Std dev (2σ)	60	38	32	30
Water (nm)	Max	116	102	115	99
	Std dev (2σ)	116	62	58	50

The data in this work were analyzed using a third-order fit to relate LCI sensor reading to spatial depth due to the reliability of fit over the range of operation without overfitting the dataset.

4 Step Height Measurements

To demonstrate the effectiveness of the sensor probe in air and water in terms of accuracy and precision, step height measurements were performed. Ten consecutive line scans across the same 4-mm section of a 8-, 7-, 6-, and 5-μm step height were achieved by laterally translating the sample in 10-μm steps while capturing 20 consecutive spectra at each location for signal averaging. In accordance with Eq. (3), the refractive index of water was taken into account using a value of $n = 1.33$ to compensate for increased path length difference when operating submerged in water due to the increase in refractive index while maintaining use of air calibration.

The measurements in air were taken with the stand-off distance of between 161.3 and 336.6 μm and in water with a stand-off of 195.6 to 371.4 μm as shown by the bands enclosed within the dotted vertical lines in Fig. 4. This operation region was chosen as it is a common stand-off distance during EJM processing. The range of step heights has also been selected to demonstrated the performance capability of such a sensor for measuring micrometer scale structures in both air and submerged in water. Figure 6 shows the mean step profile generated from the 10 line scans over a set of slip gauges of varying step height measured in air; the same measurements were also made in water as shown in Fig. 7. This mean achieved measurement for each step height in air and water along with the 2σ standard deviation can be seen in Table 2, with the nominal value referring to the predicted step height from the wringing of two slip gauges such that the difference in thickness equates to the nominal value.

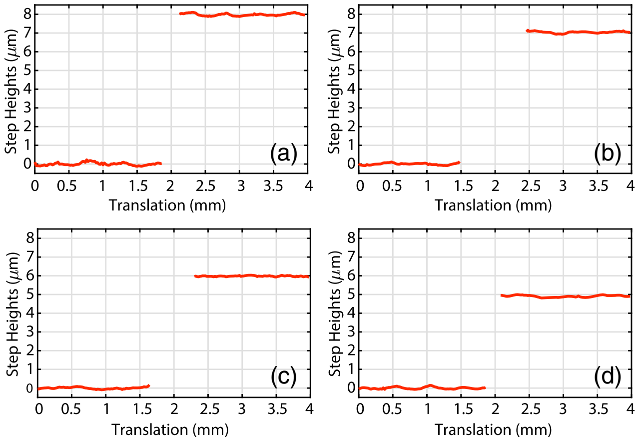

Fig. 6 Measured step height profiles in air: (a) 8 μm, (b) 7 μm, (c) 6 μm, and (d) 5 μm.

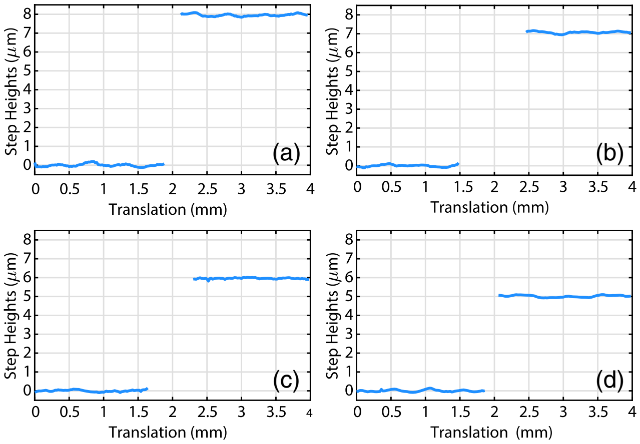

Fig. 7 Measured step height profiles in water: (a) 8 μm, (b) 7 μm, (c) 6 μm, and (d) 5 μm.

Table 2 Measured step height profiles in air and water. All values in μm.

Nominal	Mean	(2σ) Std dev	Environment
8	7.91	0.018	Air
	7.97	0.026	Water
7	7.07	0.056	Air
	7.08	0.032	Water
6	5.86	0.024	Air
	5.91	0.076	Water
5	4.96	0.038	Air
	4.97	0.048	Water

It can be seen that although the profiles are centered around their respective nominal step height values there is some oscillations present in the obtained profile across both air and water datasets. This is due to the ball screw oscillation movement introduced using the Newport motorized linear stages, which shows a repeatable mean oscillation of ±200 nm with a pitch of 490 μm independent of operating medium.

From Fig. 8, it can be seen that a tight spread of height measurements was achieved across all step height measurements indicating a high confidence in precision and repeatability of absolute

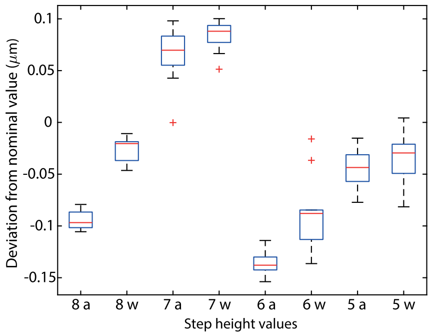

Fig. 8 Deviation of measured step heights from nominal value in air (a) and water (w). The red "+" symbols indicate outlier values.

depth measurement within the measured region. It can also be seen from the box plots and the tabulated data in Table 2 that, when transferring from operating in air to water medium, the achieved depth value changes, with a slight increase in measured step height shown even after compensating for the increased OPD due to increased refractive index of the medium by dividing measured depths with the value $n = 1.33$. The data show a tendency to have a reduced measurement precision when operating in water. However, this is not always seen as in the case of the 7-μm step height, here it is partially due to an outlier value as shown in Fig. 8, which was taken into consideration during calculation of standard deviation of the dataset in Table 2.

5 Conclusion

The application of a lensless fiber-based LCI for use in industrial metrology applications has been demonstrated, with evaluation of sensor performance across standard and nonideal operating conditions. This system has been used to measure step height changes on metallic surfaces in both air and water. An analysis of the system performance in different regions of operation has been conducted. This has shown the device to be approximately linear in performance with deviations from a first-order polynomial fit of the order ±50 nm in air and ±100 nm in water, quantifying the applicability of this technology for use in an *in-situ* measurement configuration. Characterization of system performance in air and water media has been demonstrated with a range of slip gauge step heights (8, 7, 6, and 5 μm), with significant similarity of achieved measurement between medium operation and a minimum 2σ precision of ±56 nm in air and ±76 nm in water. This work will now extend to analyze the impact of sample surface roughness and microtextures on the sensor's ability to resolve depth and surface features as a step toward expected operational procedure in an *in-situ* measurement scenario. In addition, different media with varying refractive index, such as mineral oil and glycerine, will be tested.

Acknowledgments

The authors wish to acknowledge support of the UK Engineering and Physical Sciences Research Council (EPSRC) for funding this work (Grant Nos. EP/M020746/1 and EP/L01498X/1). The authors declare that there are no conflicts of interest related to this article.

References

1. K. Michael et al., "Optical coherence tomography," *Optik Photonik* **4**(4), 24–28 (2009).
2. L. Hungyen et al., "A review of the applications of OCT for analysing pharmaceutical film coatings," *Appl. Sci.* **8**(12), 2700 (2018).
3. F. Karim et al., "Optical fiber-based sensor for in situ monitoring of cadmium sulfide thin-film growth," *Opt. Lett.* **38**(24), 5385–5388 (2013).
4. J. Krauter and W. Osten, "Nondestructive surface profiling of hidden MEMS using an infrared low-coherence interferometric microscope," *Surf. Topogr. Metrol. Prop.* **6**, 015005 (2018).
5. D. Tang, F. Gao, and X. Jiang, "On-line surface inspection using cylindrical lens-based spectral domain low-coherence interferometry," *Appl. Opt.* **53**, 5510–5516 (2014).
6. P. Tuukka et al., "Optical coherence tomography as an accurate inspection and quality evaluation technique in paper industry," *Opt. Rev.* **17**, 218–222 (2010).
7. H. M. Park, H. W. Jung, and K.-N. Joo, "Dual low coherence scanning interferometry for rapid large step height and thickness measurements," *Opt. Express* **24**, 28625–28632 (2016).
8. H. M. Park and K.-N. Joo, "High-speed combined NIR low-coherence interferometry for wafer metrology," *Appl. Opt.* **56**, 8592–8597 (2017).
9. A. Di Donato et al., "Infrared imaging in liquid through an extrinsic optical microcavity," *Opt. Lett.* **38**(23), 5094–5097 (2013).

10. A. Majumdar and H. Huang, "Development of an in-fiber white-light interferometric distance sensor for absolute measurement of arbitrary small distances," *Appl. Opt.* **47**(15), 2821–2828 (2008).
11. J. Mitchell-Smith, A. Speidel, and A. Clare, "Transitory electrochemical masking for precision jet processing techniques," *J. Manuf. Processes* **31**, 273–285 (2018).
12. K. M. Tan et al., "In-fiber common-path optical coherence tomography using a conical-tip fiber," *Opt. Express* **17**, 2375–2384 (2009).
13. R. Leitgeb, C. K. Hitzenberger, and A. F. Fercher, "Performance of Fourier domain vs. time domain optical coherence tomography," *Opt. Express* **11**, 889–894 (2003).
14. M. E. Brezinski, *Optical Coherence Tomography: Principles and Applications*, Elsevier, London (2006).
15. X. Liu et al., "Towards automatic calibration of Fourier-domain OCT for robot-assisted vitreoretinal surgery," *Opt. Express* **18**, 24331–24343 (2010).
16. W. Drexler and J. G. Fujimoto, *Optical Coherence Tomography: Technology and Applications*, Springer Science and Business Media, Berlin, Heidelberg (2008).
17. C. Dorrer et al., "Spectral resolution and sampling issues in Fourier-transform spectral interferometry," *J. Opt. Soc. Am. B* **17**, 1795–1802 (2000).
18. M. Wojtkowski et al., "*In vivo* human retinal imaging by Fourier domain optical coherence tomography," *J. Biomed. Opt.* **7**(3), 457–463 (2002).
19. D. Hillmann, G. Httmann, and P. Koch, "Using nonequispaced fast Fourier transformation to process optical coherence tomography signals," *Proc. SPIE* **7372**, 73720R (2009).
20. Z. Hu and A. M. Rollins, "Fourier domain optical coherence tomography with a linear-in-wavenumber spectrometer," *Opt. Lett.* **32**, 3525–3527 (2007).
21. A. Payne and A. G. Podoleanu, "Direct electronic linearization for camera-based spectral domain optical coherence tomography," *Opt. Lett.* **37**, 2424–2426 (2012).
22. M. Mujat et al., "Autocalibration of spectral-domain optical coherence tomography spectrometers for *in vivo* quantitative retinal nerve fiber layer birefringence determination," *J. Biomed. Opt.* **12**(4), 041205 (2007).
23. X. Zhang et al., "Self-spectral calibration for spectral domain optical coherence tomography," *Opt. Eng.* **52**(6), 063603 (2013).
24. J. Kim, J. Han, and J. Jeong, "Accurate wavelength calibration method for spectrometer using low coherence interferometry," *J. Lightwave Technol.* **33**, 3413–3418 (2015).
25. J.-H. Kim, J.-H. Han, and J. Jeong, "Wavelength calibration of dispersive near-infrared spectrometer using relative k-space distribution with low coherence interferometer," *Opt. Commun.* **367**, 186–191 (2016).
26. C. Ding et al., "A new spectral calibration method for Fourier domain optical coherence tomography," *Optik* **121**(11), 965–970 (2010).
27. H. Hamid and C. R. Carla, "Numerical study on spectral domain optical coherence tomography spectral calibration and re-sampling importance," *Photonic Sens.* **3**, 35–43 (2013).
28. D. J. Faber and T. G. van Leeuwen, "Doppler calibration method for spectral domain OCT spectrometers," *J. Biophotonics* **2**(67), 407–415 (2009).
29. M. Szkulmowski, S. Tamborski, and M. Wojtkowski, "Wavelength to pixel calibration for Fdoct," *Proc. SPIE* **9312**, 93123L (2015).
30. C. N. Copeland and A. K. Ellerbee, "Analysis of the effects of different resampling techniques for optical coherence tomography," *Proc. SPIE* **8227**, 82270W (2012).
31. J. Ke and E. Y. Lam, "Image reconstruction from nonuniformly spaced samples in spectral-domain optical coherence tomography," *Biomed. Opt. Express* **3**, 741–752 (2012).
32. M. Jeon et al., "Full-range k-domain linearization in spectral-domain optical coherence tomography," *Appl. Opt.* **50**, 1158–1163 (2011).
33. B. Adrian et al., "Recovering distance information in spectral domain interferometry," *Sci. Rep.* **8**(1), 15445 (2018).

Tom Hovell received his BEng degree in mechanical engineering in 2015 followed by an MSc degree in mechanical engineering in 2017 both from Loughborough University. In late 2017, he began his PhD in low-coherence interferometry for *in-situ* metrology at Loughborough

University. His research interests include optical sensor systems integration, surface profilometry, interferometry, and *in-situ* metrology.

Ranveer S. Matharu received his PhD in electrical engineering from the University of Queensland Australia in 2012. He held a research associate position at Loughborough University and is now currently based at Coventry University. His research interests are imaging and sensing via a wide range of optical techniques. His current work focuses on supporting the electric revolution through the integration of metrology and their systems within the manufacturing environment to provide new ways of automation.

Jon Petzing received his degree and PhD at Loughborough University before joining the academic staff in 1996 as the National Physical Laboratory Lecturer in Optical Engineering. His research is concerned with dimensional, surface, optical, acoustic, and pressure metrology, as well as the emerging field of biometrology and metrology standards. These are predominantly in the context of high value manufacturing engineering, with over 150 journal, conference and other publications within the field.

Laura Justham gained a first class masters of physics degree in 2003 and received her PhD in manufacturing systems engineering in 2007, both from Loughborough University. Following various PDRA positions, she took up her lectureship in manufacturing processes and intelligent automation systems in 2012. Her research interests include manufacturing process engineering, especially within complex manufacturing environments and emerging technologies. She is currently focused on intelligent sensing to support process adaptivity and autonomy.

Peter Kinnell received an MEng degree in mechanical engineering from the University of Birmingham in 2001. He remained at Birmingham gaining a PhD in microelectromechanical systems (MEMS) in 2005. He then worked for GE sensing on the design of high-performance MEMS sensors, before moving back to academia in 2010. He is currently a senior lecturer at Loughborough University, working on metrology to support manufacturing and automation, including 3-D machine vision, *in-situ* metrology, and robot-mounted sensors.